SANDIA REPORT
SAND2006-6561
Unlimited Release
Printed October 2006

Hydrodynamic Effects on Coalescence

Anne M. Grillet, Carlton F. Brooks, Maarten P. De Boer, Chris J. Bourdon, Thomas G. Dimiduk, Tom A. Baer, Allen D. Gorby and Michael Loewenberg

Prepared by
Sandia National Laboratories
Albuquerque, New Mexico 87185 and Livermore, California 94550

Sandia is a multiprogram laboratory operated by Sandia Corporation,
a Lockheed Martin Company, for the United States Department of Energy's
National Nuclear Security Administration under Contract DE-AC04-94AL85000.

Issued by Sandia National Laboratories, operated for the United States Department of Energy by Sandia Corporation.

Available to DOE and DOE contractors from
U.S. Department of Energy
Office of Scientific and Technical Information
P.O. Box 62
Oak Ridge, TN 37831

Telephone: (865) 576-8401
Facsimile: (865) 576-5728
E-Mail: reports@adonis.osti.gov
Online ordering: http://www.osti.gov/bridge

Available to the public from
U.S. Department of Commerce
National Technical Information Service
5285 Port Royal Rd.
Springfield, VA 22161

Telephone: (800) 553-6847
Facsimile: (703) 605-6900
E-Mail: orders@ntis.fedworld.gov
Online order: http://www.ntis.gov/help/ordermethods.asp?loc=7-4-0#online

SAND2006-6561
Unlimited Release
Printed October 2006

Hydrodynamic Effects on Coalescence

Anne M. Grillet[*], Carlton F. Brooks[†], Maarten P. De Boer[‡], Chris J. Bourdon[*], Thomas G. Dimiduk[†], Tom A. Baer[^] and Allen D. Gorby[*]

[*]Microscale Science and Technology
[†]Thermal, Fluid and Aero Experimental Sciences
[‡]MEMS Devices & Reliability Physics
[^]Multiphase Transport Processes
Sandia National Laboratories
P.O. Box 5800, MS 0834
Albuquerque, New Mexico 87185-0834

Michael Loewenberg
Department of Chemical Engineering
Yale University
PO Box 208286
New Haven, CT 06520-8286

Abstract

The goal of this project was to design, build and test novel diagnostics to probe the effect of hydrodynamic forces on coalescence dynamics. Our investigation focused on how a drop coalesces onto a flat surface which is analogous to two drops coalescing, but more amenable to precise experimental measurements. We designed and built a flow cell to create an axisymmetric compression flow which brings a drop onto a flat surface. A computer-controlled system manipulates the flow to steer the drop and maintain a symmetric flow. Particle image velocimetry was performed to confirm that the control system was delivering a well conditioned flow. To examine the dynamics of the coalescence, we implemented an interferometry capability to measure the drainage of the thin film between the drop and the surface during the coalescence process. A semi-automated analysis routine was developed which converts the dynamic interferogram series into drop shape evolution data.

ACKNOWLEDGMENTS

The authors would like to acknowledge the efforts of Mike Prairie in the conception and funding of this project and the assistance of Thomas Grasser with support designing and constructing the flow chamber.

CONTENTS

FIGURES

TABLES

NOMENCLATURE

C*n*	Camera (1-2)
FC	flow cell
$f_{x'}$, $f_{y'}$ I	deviation functions for measuring the error in the position of the droplet used in the control algorithm
I_n	intensities of the reflected light beams (1,2)
I_{av}	average intensity of the interference pattern
I_{amp}	amplitude of the interference pattern
I_{max}, I_{min}	interference pattern intensity at the maximum and minimum respectively
K_P,K_I	proportional integral control parameters
LA	linear actuator
LR	lower reservoir
n_d	refractive index
PB	polybutadiene (phenyl terminated)
PDMS	polydimethylsiloxane
p	pressure
r	radial unit vector in x-y plane
PIV	particle image velocimetry
PP	peristaltic pump
PV*n*	proportioning valves (a-d)
R_{max}	distance when proportional integral control initiated
S	microsyringe
SP	syringe pump
T	tee
u	velocity
UR	upper fluid reservoir
V	three way manual valve
w	relative height
x, y	horizontal coordinates in camera reference frame
x', y'	horizontal coordinates in exit port reference frame
x_0, y_0	center coordinates in camera reference frame
v	component of velocity vector in the x-y plane
λ	wavelength of interferometer illumination
η	matrix fluid viscosity
θ	radial uniformity parameter
π	Pi
ϕ	phase angle of interference fringe

1. INTRODUCTION

Dispersed emulsions are complex fluid systems encountered in paints, food industries, polymer production and many other applications. Dispersion of one fluid phase into another allows manipulation of fluid properties such as thermal expansion, electrical and thermal conductivities as well as strength and toughness of cured polymers through control of the droplet microstructure. These dispersions are finding many exciting new applications in areas of self-assembled nano-structured materials and manufacturing of novel optical materials. The properties of these materials depend strongly on the morphology of the dispersed phase, which in turn depends on the microstructure formation and destruction through drop break up and coalescence.

Coalescence is the process by which two smaller droplets are brought into contact and merge into one larger droplet. In many cases, the rate limiting step that determines if the two droplets will combine is the drainage of the fluid from between the two approaching surfaces. The physics of coalescence are very complex because the macroscale behavior is controlled by the small scale dynamics in the draining film. For drops that are millimeters in diameter, the fluid between the droplets must be squeezed out until the thin film is around 100 nm thick before the van der Waals forces become strong enough to cause the two drops to merge. This range of lengths scales has made it very difficult to apply traditional continuum modeling techniques to understand the dynamics of coalescence. In addition, many of the interesting applications where coalescence is a determining factor usually include other complicating factors such as an external flow or surface-active materials such as surfactants.

Recently, Michael Loewenberg of Yale University proposed a theory that predicts how hydrodynamic forces can be manipulated to control coalescence.[1] This technology has great potential to impact our understanding of foam processing (both manufacture and thermal decomposition) and other core technologies for Sandia and our customers (e.g., chemical and consumer product manufacturing industries). Unfortunately, because of the large disparity of length scales between the drop size and the draining film (<1% of the drop radius), this theory has never been experimentally validated. In collaboration with Prof. Loewenberg, we have developed a controlled flow apparatus that can impose a controlled hydrodynamic force on a drop which can be coupled to an interferometry imaging system to measure the coalescence dynamics. The goal is to experimentally validate his theoretical model for hydrodynamic effects on coalescence.

1. 1. Previous Work

Much of the theoretical work on coalescence dynamics has focused on the model problem of two droplets brought together by an external driver such as gravity or a hydrodynamic drag force. A theoretical framework for coalescence was initially developed for non-deformable spherical drops with tangentially immobile interfaces (i.e. no internal flow) that assumed that the thin film between the drops was expelled due to the high pressure in the contact area between the drops. The effect of mobile interfaces was incorporated by Yiantsios & Davis (1990) and others [2], but

even more recent coalescence theories have depended on several questionable assumptions about the effect of the external flow on the coalescence dynamics:

1) The external flow is unimportant other than to act as a driving force to bring the two droplets into contact.
2) The contact region takes the form of a hydrostatic constant curvature dome at the center of the film.

Recent theoretical developments by Prof. Loewenberg have found that these basic assumptions are incorrect and can lead to incorrect predictions of coalescence events.[1] The implications of his theory are even more profound, indicating that the external flow can in fact play a controlling role in hindering or accelerating coalescence of drops in a dispersion. His recent predictions suggest that the external flow can in fact be harnessed to manipulate coalescence events. Figure 1 demonstrates how the external flow can qualitatively change the shape of the film between two approaching drops. An important challenge remains in validating Loewenberg's theoretical model through careful experimentation that incorporates hydrodynamic effects.

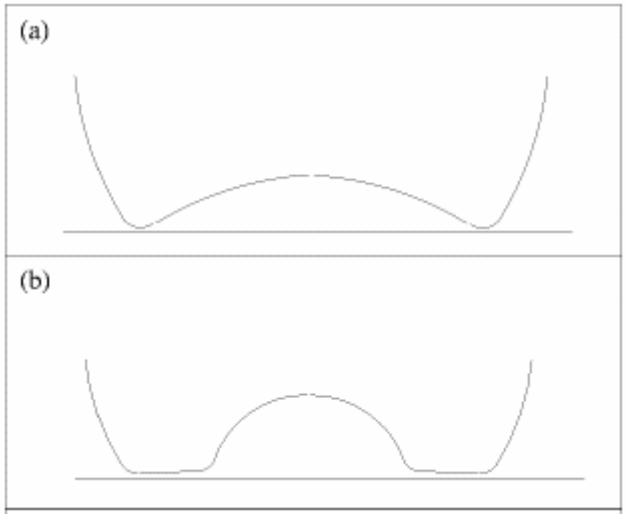

Figure 1: Intermediate film profile as two drops approach each other. The horizontal line indicates the symmetry plane. a) ambient flow negligible, b) ambient flow hinders film drainage.

Previous experimental studies have used a variety of techniques to measure the drainage of thin films and coalescence dynamics including video imaging, interferometry, electrical impedance and ellipsometric methods. Video imaging of colliding drops was employed by Guido & Simeone to determine conditions resulting in coalescence, but was not able to make accurate measurements of the small scale structure. [3] Electrical impedance has been used to study a drop approaching a reservoir of the same material, but can only provide average film thickness measurements [4]. The most common method has been interferometry which has been applied to captive approaching drops [5] and thin film drainage [6] to measure film thickness by counting interference fringes as the two drops approach each other. In the literature, interferometry has proven to be a simple, yet powerful method to accurately measure very thin films between two approaching interfaces. The film thickness resolution of interferometry is

limited by the wavelength of the laser and typically the inter-fringe spacing is on the order of several hundred nanometers. Using 'phase unwrapping' techniques, the height resolution can increase to 10's of nanometers under ideal conditions.[7,8] Another promising optical method to determine film thickness is ellipsometry which has the capability to improve resolution by incorporating phase information.[7,10] Due to the very thin films which develop during a coalescence event, novel experimental techniques that can measure detailed two dimensional film thickness profiles accurately down to 10s of nanometers are required in order to compare between competing theoretical models. Also, many of the experiments performed to date have focused on drainage of an isolated thin film and captive drop studies that cannot be easily adapted to study hydrodynamic effects on coalescence.

1. 2. Technical Approach

We have developed a strategic collaboration with Prof. Loewenberg to validate his new theories on hydrodynamic manipulation of coalescence and create novel experimental methods to probe coalescence dynamics. Previous experimental work has not been able to provide the kind of high fidelity, high resolution data needed to distinguish between competing theories of drop coalescence dynamics. Experiments studying hydrodynamic effects using video imaging of colliding drops were too coarse to distinguish the small scale dynamics in the film which control coalescence. Earlier measurements of film drainage dynamics have not been designed to investigate hydrodynamic effects. Our experiments have created a novel flow experiment which can guide a drop through an axisymmetric compression flow towards a static surface. A drop approaching a static surface is an analog to two drops approaching each other. Both situations exhibit the same physics (with slightly different scaling laws) but using a static surface allows easy optical access to the thin film which forms between the two interfaces. Then interferometry can be used to measure the dynamics of the drainage of the thin film region.

The greatest technical challenge of this work has been developing a computer controlled flow system that can reliably steer the drop to the detection region of the interferometer. Such systems have been previously developed for holding a drop or particle at the center of a two dimensional extensional flow, but only for observation with video imaging. Those efforts only required positioning control along one axis, while we will require two axis positioning control to generate a biaxial compression flow. Because our goal is to position the drop and perform interferometry, the drop will need to be positioned with greater precision than previous implementations. To understand the hydrodynamic effects on coalescence dynamics, we also need to create a close approximation to ideal axisymmetric flow in the region around the drop. With design guidance from finite element simulations, we have developed a flow cell and a real time computer control system to create and control the flow. We have also confirmed the performance using particle image velocimetry to measure the velocity and radial uniformity of the flow.

While the basic interferometry technique is well understood [7,8], applying this technique to understand coalescence dynamics requires careful implementation. One of the main challenges involves tracking the drop shape through a topology change (from a round drop to a dimpled shape). Also, a study of the dynamics requires an efficient technique to process significant amounts of data. To this end we have developed a semi-automated program which prompts the

user for guidance at critical points but enables an interferogram series of 200 images to be processed in under an hour.

2. FLOW CELL AND DROP CONTROL

Developing the flow cell and control system was a critical step in understanding the effects of hydrodynamic forces on coalescence. Our design was based on creating a three dimensional extension of the two dimensional controlled extensional flows which have been discussed in the literature [11]. Because of the inherent three dimensional nature of the flow, wall effects can have a significant impact. Ensuring that the region around the center symmetry axis experienced near ideal compression flow was important for our goal of studying the effect of hydrodynamics on coalescence. Thus, before building a prototype, we performed finite element simulations of our preliminary design. We then took that knowledge and built a controlled flow system. We have demonstrated that system and characterized the flow properties using particle image velocimetry in this section.

2. 1. Finite Element Calculations for Design Guidance

Calculations were performed using our finite element code Goma assuming negligible inertia (i.e. Stokes flow), incompressible fluid, Newtonian rheology and steady flow. Thus the governing equations of motion are

$$\nabla \cdot \vec{u} = 0$$
$$\nabla p = \eta \nabla^2 \vec{u} \qquad [1]$$

where $\vec{u}$ is the velocity, p is the pressure and η is the viscosity of the fluid. Since Stokes flow is linear, the applied velocity is arbitrary. Figure 2 shows the preliminary design for the flow cell which consists of a box 50mm square and 25mm tall. The inlet is a 6mm hole in the center of the top and there are four outlets, one in each bottom corner. The four outlets allow control of the drop position in two dimensions. Figure 2 shows the paths traced out by many particles introduced into the flow at the inlet. Clearly the flow is not completely axisymmetric because the flow is channeled into the outlets at the bottom corners, but for a region in the center of the cell, the wall effects are small and the flow approaches ideal biaxial compression or stagnation flow.

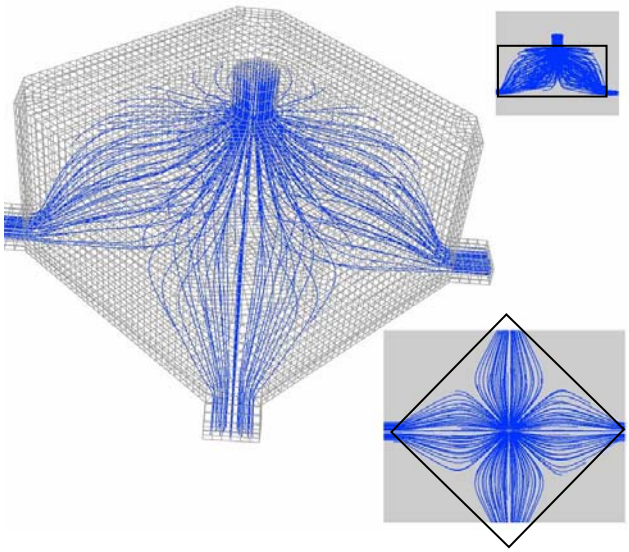

Figure 2: Paths of tracer particles released at the inlet to the flow cell. Approximate size and orientation of the flow chamber is indicated by the boxes.

Making sure that the flow is axisymmetric near the center of the flow cell is important for the validity of the experiments. Thus, we defined a radial uniformity parameter θ to quantify how axisymmetric the flow is.

$$\theta = \frac{|v \cdot r|}{|v|} \qquad [2]$$

where v is the projection of the velocity in the x-y plane (i.e. parallel to the bottom surface) and r is the radial unit vector. If the flow is axisymmetric, the planar component of the velocity would be collinear with the radial unit vector and θ=1. Figure 3 shows the radial uniformity on a cross section of the flow cell near the bottom surface where the wall effects are the strongest. The eight symmetry planes of the flow are apparent and the deviation from axisymmetric flow near the walls is quite clear. The white contour indicates the region in the center of the flow where the flow is more than 99% radial. This was quite satisfactory since it encompasses almost 25% of the width of the cell (~12mm) and our experimental drops are ~1mm in diameter.

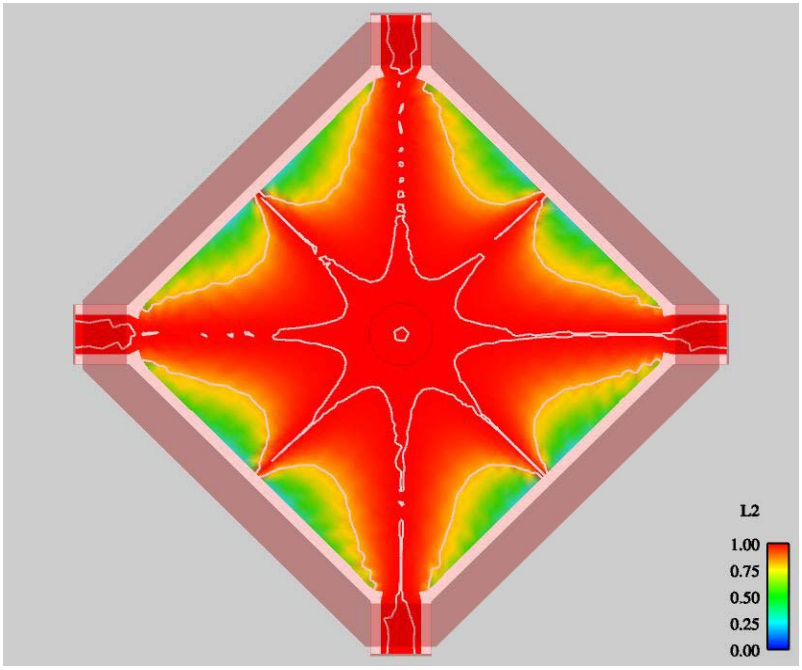

Figure 3: Radial uniformity in the flow cell. The region enclosed by the white lines represents the region of the flow where the tangential velocity is >99% radial. The artifact at the center is caused because the planar velocity *v* is identically zero and the radial unit vector is not well defined.

2. 2. Final Flow Cell Design and Experimental Materials

For the construction of the flow cell, some modifications of the preliminary design were made, primarily switching from a square cross-section to a round cross-section. This simplified certification of the design as a pressure vessel. Figure 4 shows the final constructed flow cell. The walls were constructed of acrylic to allow observation of the trajectory of the drop. Four exit ports of 3.5mm ID were placed on the cardinal points. The top and bottom of the cell were constructed of 12mm thick aluminum. The top included a 5mm ID inlet port. In order to help remove air from the cell, a slight angle was machined into the top of the flow cell. The bottom contained a machined cut out for an acrylic window. The window had a top hat shape so that the view of the bottom of the flow cell was not obstructed by the o-ring used to seal the cell (shown in black). O-rings were also used to seal the top and bottom of the cell but are not shown in Figure 4 for clarity.

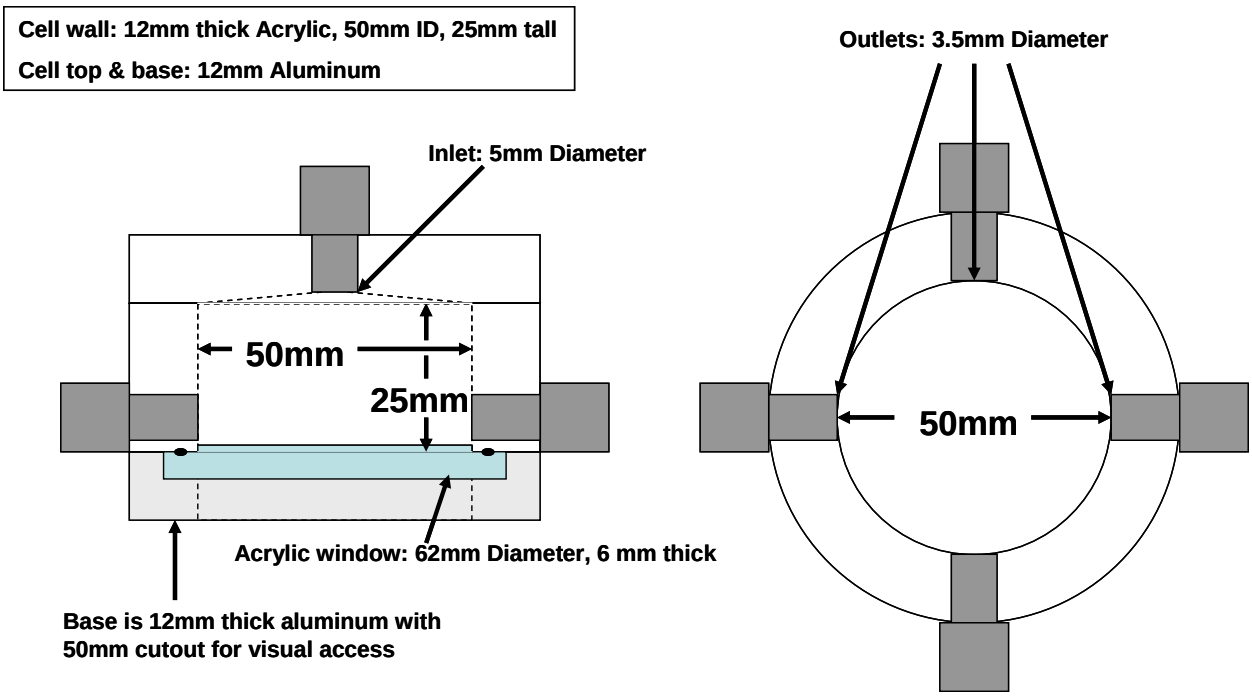

Figure 4: Design for constructed flow cell including critical dimensions.

The choice of drop and matrix fluid materials for this experiment was critical for the success of the coupled experiments. For good contrast with the interferometry, the refractive index differences across the surface – matrix fluid interface and matrix fluid – drop fluid interface must be matched and maximized. We also wanted to eliminate the effects of inertia in our experiments by operating with high viscosity and slow flow. For the interferometry experiments, the drop material is poly (butadiene) (PB – Acros Organics) and the matrix fluid is poly (dimethylsiloxane) (PDMS – Dow Corning 200 1000 cSt). The materials have refractive indices n_d =1.50 and n_d =1.40 respectively.[12] However, for development of the flow control system, we needed a system where the drop would not coalesce with the bottom interface. Thus initial testing used a drop phase of deionized water with a matrix material of poly (propylene glycol) (M_w=4000, Polysciences, Warrington, PA). Materials were used as received from the manufacturer.

2. 3. Flow Control System Design

A block diagram of the flow system used for our experiments is depicted in Figure 5. The liquid used for the continuous phase was initially loaded into an upper reservoir. This was connected to a three-way valve that connected the upper reservoir to a syringe pump and the flow cell. With a filled upper reservoir, a Harvard Apparatus PHD 22/2000 Remote Syringe Pump (Holliston, MA) was primed when the three-way valve was set to refill. Once the syringes were primed, the three-way valve was set to deliver fluid to the flow cell at the desired volumetric flow rate. The flow direction and flow rate for the syringe pumps were controlled remotely using an RS-232 serial interface.

Inserted in the flow path between the syringe pump and the flow cell entrance was a custom machined acrylic tee that was coupled to a motorized syringe for injection of droplets into the continuous phase. The motorized syringe consisted of a microsyringe that used disposable borosilicate capillaries (Drummond Scientific, Broomall, PA; Model: 25uL Dialamatic Microdispenser) coupled to a linear actuator (Zaber Technologies, Inc., Richmond, BC; Model: LA60A) to drive the syringe plunger. The tip of the capillary was inserted approximately into the middle of the flow path and typically drops from 0.5 to 2uL were injected into the flowing stream. The viscous drag on this drop was sufficient to detach it from the capillary and progress downstream into the flow cell. Commands to inject droplets were sent to the actuator by means of another RS-232 serial interface.

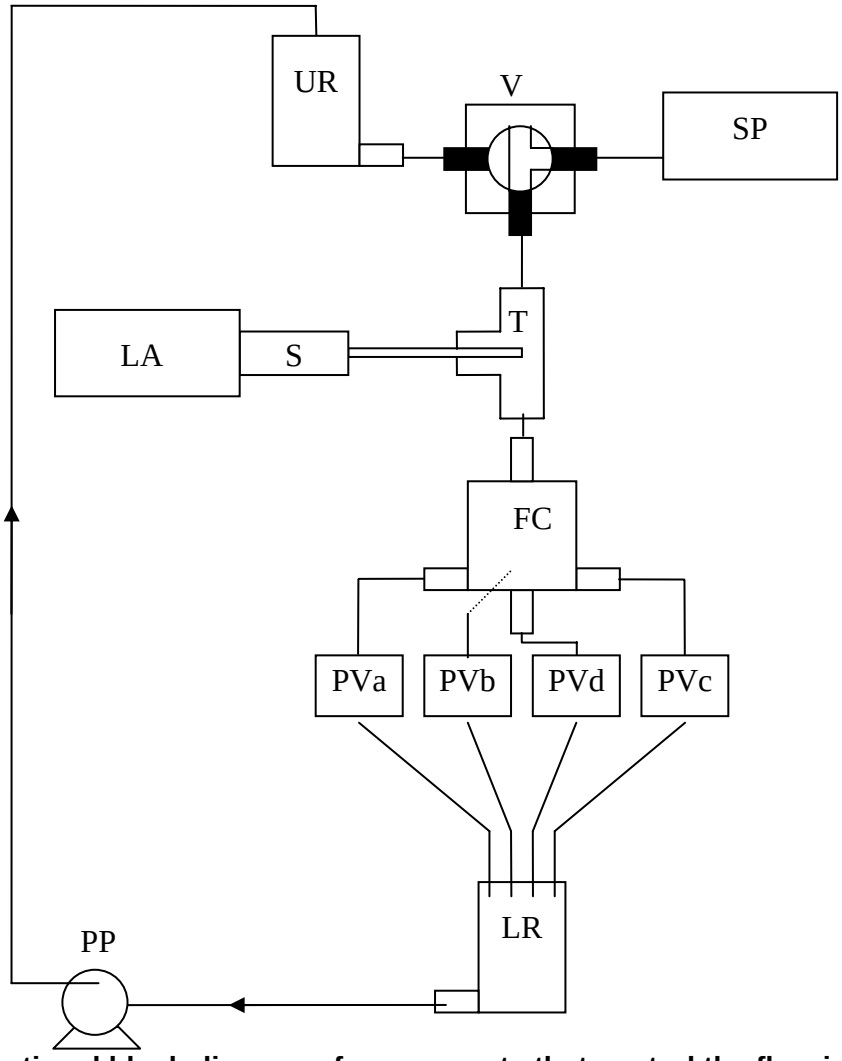

Figure 5: Functional block diagram of components that control the flow in the experiment. The components are: upper reservoir (UR), three-way manual valve (V), syringe pump (SP), tee (T), microsyringe (S), linear actuator (LA), flow cell (FC), proportioning valves (PV*n*), lower reservoir (LR), and peristaltic pump (PP). Only three of the four outlets at the bottom of the flow cell are drawn.

In normal operation, the liquid was infused into the top port of the flow cell and exited through the four exit ports at the bottom of the flow cell. The flow from each exit port was routed through a proportioning solenoid valve (Model: PSV5S-VAA; Aalborg Instruments & Controls, Inc., Orangeburg, NY) prior to recombining into a collection reservoir. These valves were used to alter the flow resistance and consequently alter the flow profile inside the flow cell, allowing us to steer the drop. Inside the valves the fluid made contact with stainless steel components (Types 316 and 416) and Viton® o-rings. Using four pulse width modulated driver modules (Model: PSV-D-A; Aalborg Instruments & Controls, Inc., Orangeburg, NY) we controlled the amount that each valve was open using a 16-bit 5VDC signal generated by a NI-6704 analog output board from National Instruments (Austin, TX). All analog output levels and serial communications mentioned above were performed using custom software written in LabVIEW (National Instruments, Austin, TX).

The flow response for each valve was determined by measuring the flow rate of water at different valve settings. For this measurement water was directed from the upper reservoir, through a rotameter (McMaster-Carr, Santa Fe Springs, CA) and through each valve. This simplified flow path was used to exclude the effects of the flow cell and focus on individual valve behavior. The volumetric flow rate versus percent open is shown in Figure 6 for all four valves. The percent open is the *nominal* amount that each valve is open based on the analog control signal sent to the valve. The response for the valves all exhibit qualitatively similar behavior: a plateau when nearly fully open indicating that the tubing resistance is limiting the flow rate; a linear region where the valves are the most resistive component in the flow path; and, in some cases, a zero flow flat region in the nearly closed state. This occurs because the solenoid in the valve has to overcome the springs which maintain the valve in the closed state when not powered. Quantitatively the response of each valve was different, and operation in a partially open state was restricted to the linear portion of valve response curves. Limiting operation to the linear regime facilitated the implementation of the drop control scheme.

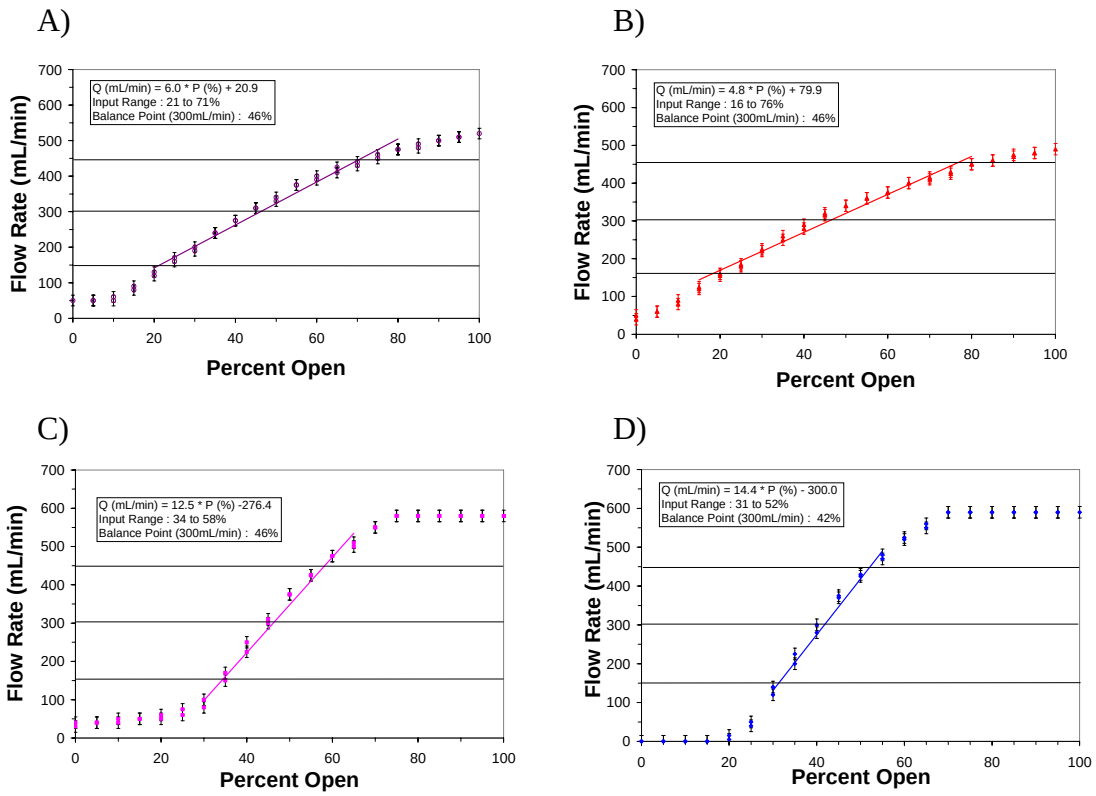

Figure 6: Water flow response curve for valve A (A), valve B (B), valve C (C), and valve D (D). When the valves were not being operated as fully opened or closed, the valves were operated in the region where the response exhibited linear behavior. This region is indicated by the line fit and the dark upper and lower horizontal lines. The dark middle horizontal line indicates the "balance point", where all valves permitted the same volumetric flow.

2. 4. Drop Tracking and Position Control

After formation of the droplet at the tee junction, it was convected into the flow cell. The position of the droplet was visualized with a pair of monochrome cameras (Watec LCL-902C), focused along the flow axis of symmetry and oriented at 90º, as shown in Figure 7. The video output from these cameras was read into a computer using two frame grabber cards (NI-1409 and NI-1407, from National Instruments, Austin, TX). The images from these two cameras were analyzed in real time at a rate of approximately 2 frames per second to determine the drop location.

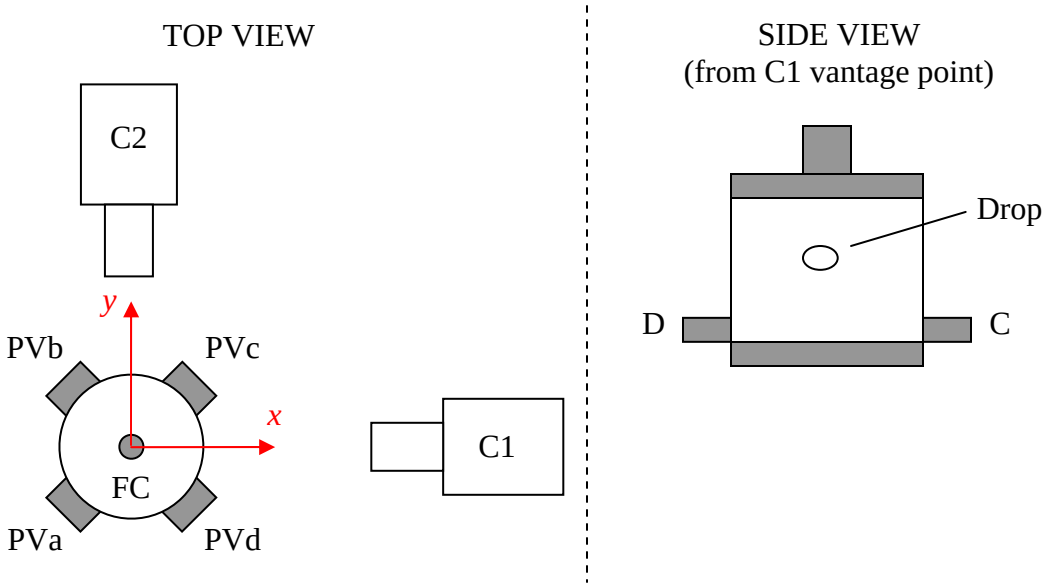

Figure 7: The left schematic shows a top view of the flow cell (FC), showing the orientation of the two cameras (C1 and C2) with respect to the exit ports (A, B, C, & D) and *xy*-coordinates. The right schematic shows an example of what the camera views. Drop size is not to scale.

To control the x-y position of the drop and steer it toward the desired x-y location a 2D control scheme was devised that included proportional and integral control. The coordinates from the camera frame of reference (*x*-*y* coordinates) were transformed to the valve (flow cell exit port) frame of reference (*x*'-*y*' coordinates) as shown in Figure 8. If the droplet was more than R_{max} pixels from the desired position, then the proportioning valves were operated in fully open/closed mode. In Figure 8, the domain is partitioned into eight sectors. If the droplet was located in one of these sectors, say sector I for example, then to pull the drop towards the center, PVa was opened and the remaining valves were closed. The valve states for all eight conditions are listed in Table 1.

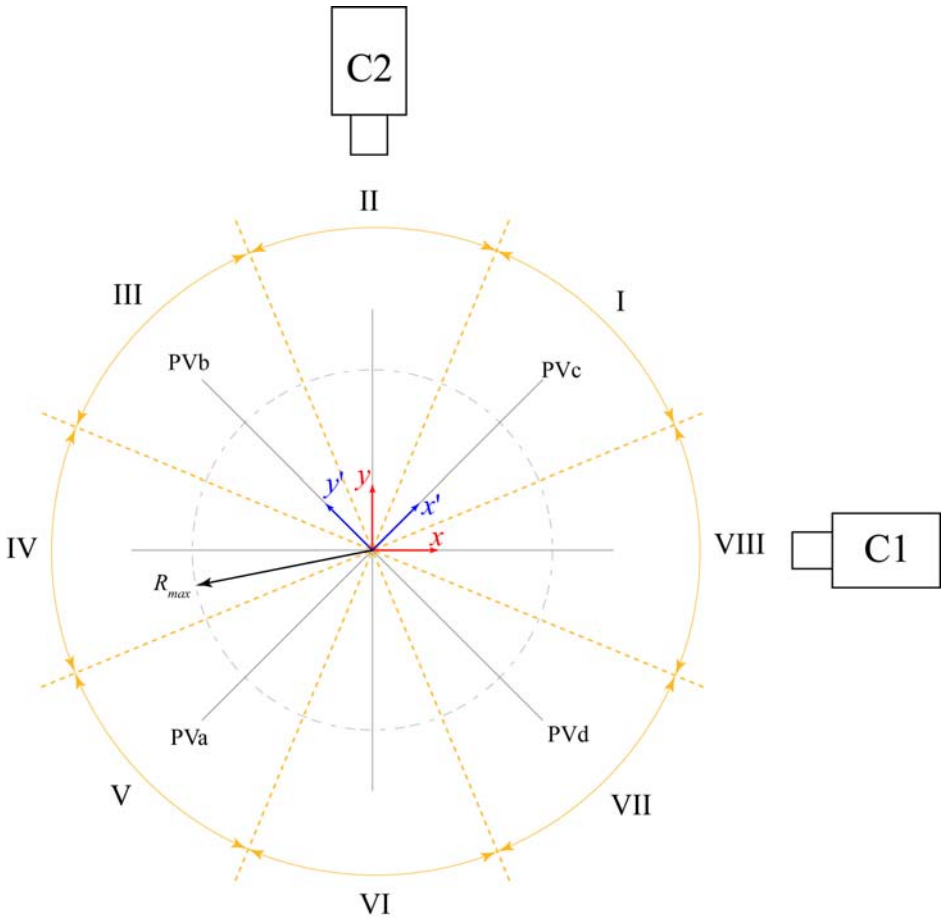

Figure 8: The left schematic shows a top view of the flow cell (FC), showing the orientation of the two cameras.

Table 1. Valve conditions when the drop was located more than R_{max} from the desired location

Sector	PVa	PVb	PVc	PVd
I	Open	Closed	Closed	Closed
II	Open	Closed	Closed	Open
III	Closed	Closed	Closed	Open
IV	Closed	Closed	Open	Open
V	Closed	Closed	Open	Closed
VI	Closed	Open	Open	Closed
VII	Closed	Open	Closed	Closed
VIII	Open	Open	Closed	Closed

When the drop was within R_{max} pixels from the desired position (x'_0, y'_0), the following control variables based on a proportional-integral control scheme were calculated

$$f_{x'} = K_P\left[\frac{\Delta x' + K_I \sum_i \Delta x'(t_i)\cdot(t_i - t_{i-1})}{R_{\max}}\right], \text{ coerced to be between -1 and 1} \quad [3]$$

$$f_{y'} = K_P\left[\frac{\Delta y' + K_I \sum_i \Delta y'(t_i)\cdot(t_i - t_{i-1})}{R_{\max}}\right], \text{ coerced to be between -1 and 1} \quad [4]$$

where K_P and K_I are the proportional and integration constants, (t_i - t_{i-1}) is the time step between successive video frames[1], and the deviation variables are $\Delta x' = x' - x'_0$ and $\Delta y' = y' - y'_0$. The control variables were then used to determine the amount (%) each valve should be opened by limiting the valves to the linear response region, as discussed earlier:

$$\begin{aligned} PVa &= f_{x'}(71-21)/2 + 46 \\ PVb &= -f_{y'}(76-16)/2 + 46 \\ PVc &= -f_{x'}(58-34)/2 + 46 \\ PVd &= f_{y'}(52-31)/2 + 41.5 \end{aligned} \quad [5]$$

When either $f_{x'}$ or $f_{y'}$ was equal to ±1, the respective valve was fully opened or closed (e.g. if $f_{x'} = 1$, then PVa=100 (fully open) and PVc=0 (fully closed)). Figure 9 depicts a drop trajectory as it is brought into the center of the flow cell validating the ability of this scheme to steer the drop to the desired central location. The flow cell can also operate in the reverse sense (i.e. with the drop moving up), but that would require a change in sign in the control loop.

A) B)

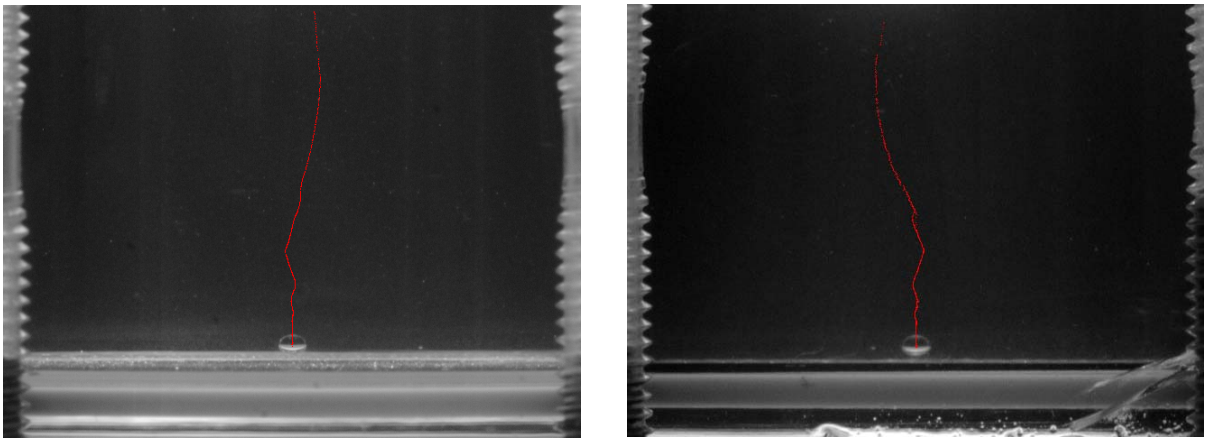

Figure 9: Trajectory of a water drop in poly (propylene glycol) as the control loop steers the drop toward the center. The drop appears as an oblate spheroid because of the curvature of the flow cell. The drop volume was 1μL, the flow rate was 1mL/min, and the control parameters are K_P = 5, K_I = 0.1s^{-1}, and R_{max} = 20 pixels.

[1] This time step is adaptive since the frame rate is not constant due to delays with performing the image analysis on non-real-time operating system (Windows XP).

2. 5. Evaluation of Flow Using Particle Image Velocimetry

Particle image velocimetry (PIV) was used in order to verify the flow symmetry within the test cell and quantify the flow effects generated by actuating the control valves. PIV is a velocity measurement technique that deduces the local flow velocity in a plane by tracking the motion of groups of particles that are seeded into the bulk flow. A series of intense, finite-duration, light pulses are formed into a thin sheet which illuminates the imaging plane, and snapshots of the particles illuminated by the laser sheet are captured by a CCD image array or other imaging system. The velocity in a defined region of the flow field (an interrogation window) is determined by comparing the relative position of a group of particles between subsequent images utilizing a cross-correlation technique, and dividing the mean displacement of that particle group by the time delay between the images. For this set of experiments, an Nd:YAG laser (Continuum, Irvine, CA model Minilite PIV, energy of 25 mJ/pulse, 4 ns pulse duration, 532 nm frequency) was used as the illumination source, and the seed particles were fluorescent microspheres (Duke Scientific, Freemont, CA, 25 micron diameter, emission at ~590 nm frequency). By using fluorescent particles, ambient illumination and laser scattering off of the test apparatus could be filtered out of the particle images, leading to higher signal-to-noise ratio and higher data fidelity. A schematic of the PIV set-up and a sample PIV image are given in Figure 10. The laser sheet was passed through the flow cell normal to the cell walls, centered approximately 3 mm above the cell floor. Because the flow still had a very strong vertical component, the laser sheet was approximately 3 mm thick to limit the number of particles exiting the illuminated plane between images. The laser sheet was imaged at a rate of 0.6 frames/sec through the floor of the cell by a CCD camera (PI Minimax DIF, Princeton Instruments, Trenton, NJ) coupled to a 105-mm Nikon macro lens. A rectangular region, approximately 40x25 mm, was imaged in the 1300x1030 pixel CCD array with the aperture set on the lens to f/8. The seed particle density was set such that each interrogation window (32x32 pixels) contained roughly 30-50 in-focus particle images. With this high level of particle seeding, valid velocity vectors could even be obtained directly under the flow inlet, where particle drop-out rates were as high as 50% due to the strong z-velocity component. An unfortunate side effect of the high seeding density is that occasionally large agglomerates of particle would sediment onto the bottom surface in the flow chamber resulting in bright spots in the raw PIV images (c.f. Figure 10).

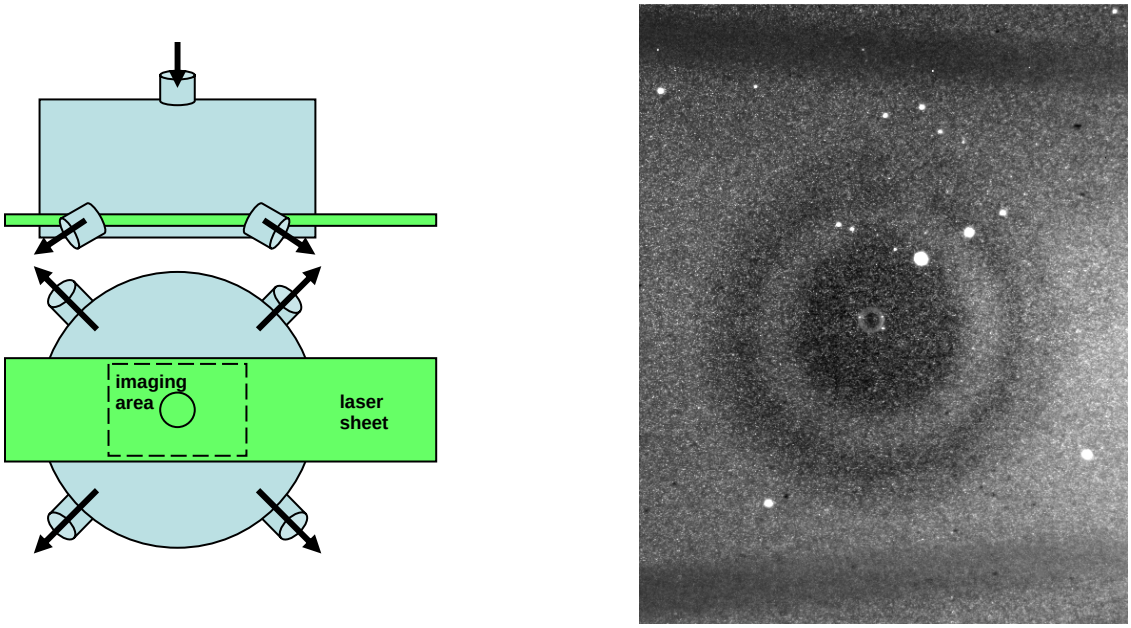

Figure 10: Location of the laser sheet through the flow cell for measuring the fluid velocity using particle image velocimetry. Right image shows a typical laser sheet image with the shadows of the mounting screws across the top and bottom, the round drop in the center of the image and the upper inlet port in the background.

We initially tested the flow characteristics of the chamber with the valves all opened to their "balanced" point as shown in Figure 6. These were the valve positions which allowed equal volumetric flow rates of water through each valve. The total volumetric flow rate through the flow cell was 2mL/min. The calculated planar velocity, v, and the radial uniformity parameter, θ, are shown in Figure 11. Since the imaging plane is centered in the flow chamber, the stagnation point should be in the center of Figure 11A. However the region where the velocity decreases to zero is shifted to the upper right indicating that the flow is not balanced. There are several potential causes for the asymmetry. Because of the higher viscosity of this fluid, there is greater viscous resistance through the valves and a larger force on the springs in the valves. Also this flow is at a much lower Reynolds number which could also affect the flow characteristics of the valves. This simply underscores the need for an active control algorithm in order to impose controlled hydrodynamics for our application.

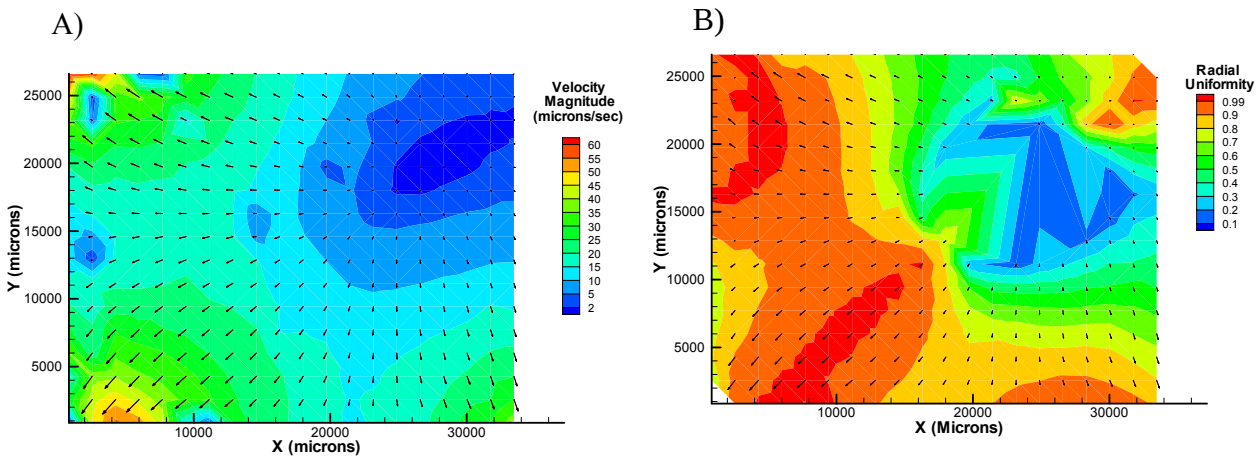

Figure 11: PIV measurement of fluid velocity in the flow cell with the valves 'balanced' as determined from the calibration shown in Figure 6. The left image shows the velocity vectors and the colors represent the magnitude of the velocity. In the right image, the colors show the radial uniformity θ.

The second series of tests were performed with the flow control scheme described above actively controlling the drop positioning as it passed through the flow cell. Unfortunately, since the laser sheet for the PIV measurements interfered with the imaging of the drop position, the control loop was disabled while the velocity measurements were taken (~1 minute). Generally, at the end of that time, the drop had only drifted a few pixels from the center axis. Figure 12 shows PIV velocity fields and the radial uniformity parameter obtained with the computer control system operating to control the flow. For this case, the velocity vectors are more uniform in the radial direction regardless of angular position up to 15 mm from the center of the inlet at the imaging plane (shown on Figure 12, right). Based on these results and several other tests at other fixed valve conditions, we can conclude that the flow cell control system is functioning as expected. Additionally, we see that the flow appears to be purely extensional in a fairly large region surrounding the stagnation point.

A) B)

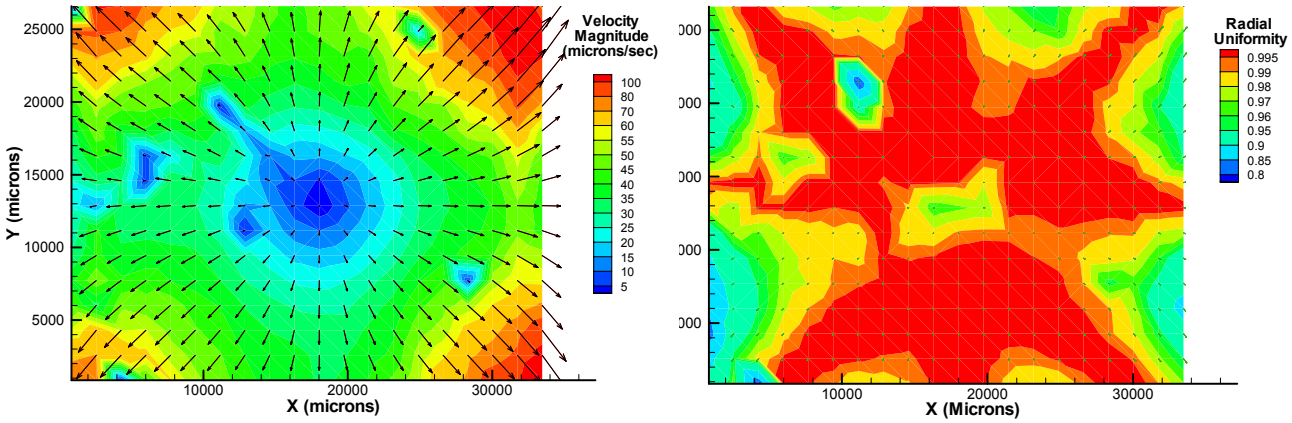

Figure 12: In plane velocity measure using PIV when the flow was controlled using the drop tracking program to ensure a symmetric flow. The left image shows the velocity vectors and the colors represent the magnitude of the velocity. In the right image, the colors show the radial uniformity θ. The edge of the orange contour shows the region with >99% radial uniformity.

3. MEASUREMENT OF COALESCENCE DYNAMICS WITH INTERFEROMETRY

Interference occurs when two coherent light waves overlap.[7] If the two light waves are of equal intensity but out of phase, destructive interference will occur and there will be no net intensity. If the two light waves are in phase, constructive interference will occur and the intensity of the two waves will be combined. This optical effect can be harnessed to make accurate small scale measurements of distances a fraction (~1/100) of the wavelength of light λ as restricted by the coherence length of the light. The coherence length L is the distance over which the light can maintain a distinct wavefront and is defined as

$$L = \frac{n\lambda^2}{\Delta\lambda} \qquad [6]$$

where n is the refractive index of the medium, $\Delta\lambda$ is the range of wavelengths. If the interaction between the two light waves occurs outside of the coherence length, then the light waves will not cause interference.

Figure 13 shows a schematic of how the interference patterns are created as a drop approaches a stationary surface. Light over a small range of frequencies ($\Delta\lambda$ =525-535 nm, L~30μm) is brought in from the bottom of the image. Because of the difference in refractive indices between the glass and the matrix fluid, some of the light reflects off of the interface (blue wave). The remaining light propagates on through the matrix fluid and some is again reflected off of the interface between the matrix fluid and the drop (red wave). Because the two interfaces are separated by the thickness of the matrix fluid layer, the two reflected light beams will be phase shifted relative to each other. Since the two interfaces are within the coherence length of the light, those phase differences will result in interference patterns. Destructive interferences (i.e. a dark fringe) will occur when the two reflections are half a wavelength out of phase. Since the film thickness is traversed twice by the second reflection, destructive interference will occur when the film thickness is one quarter of the wavelength of light. Likewise, the two reflections will be in phase (i.e. a bright fringe) if the film thickness is half of the wavelength of light. In order to maximize the contrast of the interference fringes, the refractive index differences at the two interfaces need to be well matched so that the two reflections will be of equal intensity. Note that the glass slide is ~1mm thick so that the reflection off of the bottom of the glass slide is outside the coherence length of the light and no interference will result from that reflection.

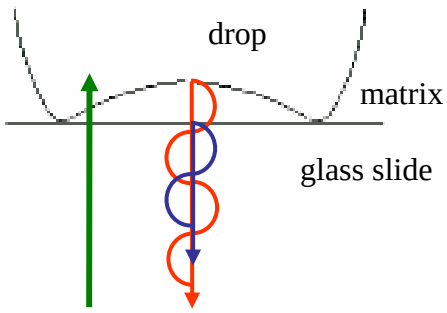

Figure 13: Schematic of interference effect from drop approach to the flat surface. The red line represents light reflecting the drop-matrix interface and the blue line represents light reflecting off of the matrix-glass interface.

In conventional phase stepping interferometry, four or five interference images (interferograms) at relative phases of $\pi/2$ are taken and well-known algorithms are used to unambiguously extract the deflection profile [10]. Phase stepping is usually accomplished by mounting the reference surface to a piezoelectric tube and moving it by $\lambda/4$ between images. The object is either static or exhibits periodic motion. In this work, Fizeau interferometry is used. The reference surface is the glass substrate and cannot be moved without distorting the experiment. Furthermore, the droplet is continuously moving. Therefore, only a single interferogram at each dimple deflection can be taken.

While the controlled flow cell was being developed, we built a small test apparatus in order to test the interferometry capability and develop the image analysis capability for dynamic time series images. Figure 14 shows a schematic of the test apparatus. Initial tests were performed with a spherical glass lens on the glass slide in air. Additionally to test the suitability of our experimental fluids for interferometry, a small fluid reservoir was placed on top of a standard microscope slide and filled with polydimethylsiloxane. A drop of polybutadiene was created on the tip of a syringe attached to a MM-3M motorized stage (National Aperture, Salem NH) and positioned inside the fluid reservoir. The interference patterns or interferograms were imaged through a Navitar UltraZoom at a fixed zoom of 3x coupled with a Mitutoyo 10x objective. Light was provided with a fiber optic source coupled into the UltraZoom. An interferometry filter (530nm, 10nm range, CVI, Albuquerque, NM) was placed in the infinity corrected optical path to increase the coherence length of the interference pattern over white light. The images were captured with a Cool Snap ES camera (Princeton Instruments, Trenton, NJ) with 12-bit dynamic range controlled through the standard control software and externally triggered with a digital delay generator (Stanford Research Laboratories, Stanford, CA, model DG-535). For the experiments shown here, the drop was moved towards the surface at a velocity of 5μm/sec.

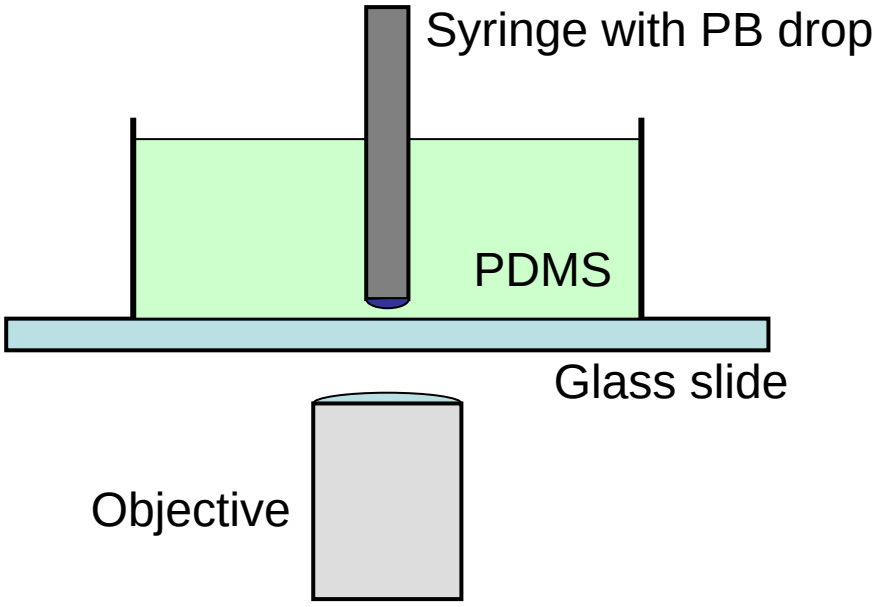

Figure 14: Apparatus to generate test data for interferometry capability.

To demonstrate the interferometry capability and the basic analysis technique, we use a topologically simpler system of a spherical glass lens held touching the top of a glass slide with air in between. The resulting interferogram is shown in Figure 15. The interference pattern shows concentric fringes which are widely spaced at the center where the lens is touching the glass slide. Further away from the center, the fringes become more closely spaced as the two glass-air interfaces diverge. The fringes are lost when the spacing exceeds the coherence length of the light source. Each of these fringes represents a constant height contour between the lower glass slide and the upper glass lens. There is a large index of refraction difference at each interface (Δn = 1.51-1 = 0.51) and the differences at the two reflecting interfaces are exactly balanced which results in clear, high contrast interference images. This interference image was taken with a smaller camera which did not have the dynamic range to capture the interference images for the liquid system.

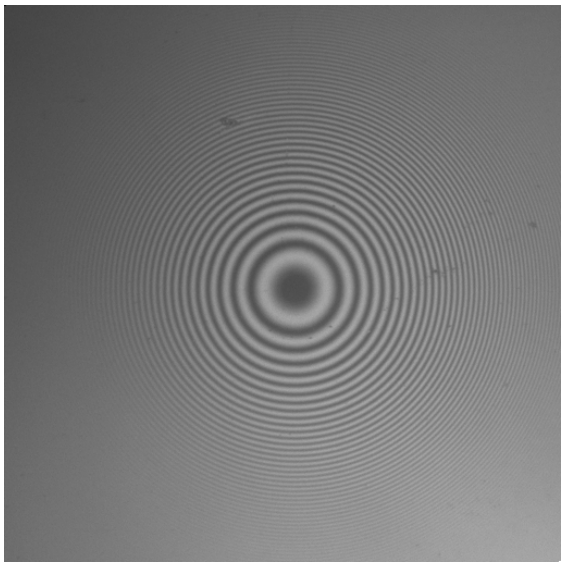

Figure 15: Interferogram for a spherical glass lens touching a glass slide with air separating the two interfaces.

The height profile can be determined using the fringes apparent in the interferogram. A horizontal line profile was taken across the image center in Figure 15, averaging over 20 rows of pixels to reduce noise. One half fringe, from one maximum to one minimum, represents a deflection of $\lambda/4$, where λ=530 nm is the illumination wavelength. Within the fringe, the intensity is

$$I = I_1 + I_2 + 2\sqrt{I_1 I_2}\sin\phi \qquad [7]$$

where I_1 and I_2 are the intensities due to beams 1 and 2 (say from the glass and the droplet surfaces) respectively, and ϕ is the phase difference between these beams [8]. This is the same as

$$I = I_{av} + I_{amp}\sin\phi \qquad [8]$$

where $I_{av} = I_1 + I_2$ and $I_{amp} = 2\sqrt{I_1 I_2}$. Note also that

$$I_{av} = (I_{\max} + I_{\min})/2 \quad \text{and} \qquad [9a]$$

$$I_{amp} = (I_{\max} - I_{\min})/2 \qquad [9b]$$

where $I_{\max}$ and $I_{\min}$ are measured local extremes in the data. Then

$$\phi = \sin^{-1}\left(\frac{I - I_{av}}{I_{amp}}\right) \qquad [10]$$

Hence within a local peak-to-valley (i.e., half a fringe), the values of I_{av} and I_{amp} can be calculated from the fringe intensity data, so ϕ is obtained at each pixel between the local maximum and the local minimum. The values of $I_{\max}$ and $I_{\min}$ often vary from fringe to fringe because illumination conditions vary across the image. Therefore, the local values within the fringe of interest are used.

If the fringe data is initially at a maximum, $\phi = \pi/2$ and the data varies as $\pi/2 \geq \phi \geq -\pi/2$ along the half fringe, the relative deflection within the half fringe is

$$w(\phi) = \pm\left(\frac{\pi/2 - \phi}{\pi}\right)\cdot\left(\frac{\lambda}{4}\right) \qquad \text{(max to min)} \qquad [11]$$

where the sign depends on if the relative deflection is up or down. Similarly, if the data is initially at a minimum, $-\pi/2 \leq \phi \leq \pi/2$, then the relative deflection within the half fringe is

$$w(\phi) = \pm\left(\frac{\phi + \pi/2}{\pi}\right)\cdot\left(\frac{\lambda}{4}\right) \qquad \text{(min to max)} \qquad [12]$$

Experimental considerations are applied to resolve the sign ambiguity. This process is known as "phase unwrapping". The deflections from adjacent half fringes of data are added to (or subtracted from) each other, with the beginning of the current half fringe being tied to the end of the previous fringe.

The experimental data and the resulting height profile are shown in Figure 16 as well as a comparison to a spherical lens shape. There is a minute deviation at the very tip of the image suggesting that the lens is not quite in contact with the glass slide. Since the fringe intensity varies significantly across the image, we needed to assume that the center fringe represented a full λ/4 distance (i.e glass in contact with glass) in order to calculate the height profile for the center fringe. The fit to a spherical lens shape suggests that the lens actually rests 18nm above the glass slide which is reasonable considering surface roughness.

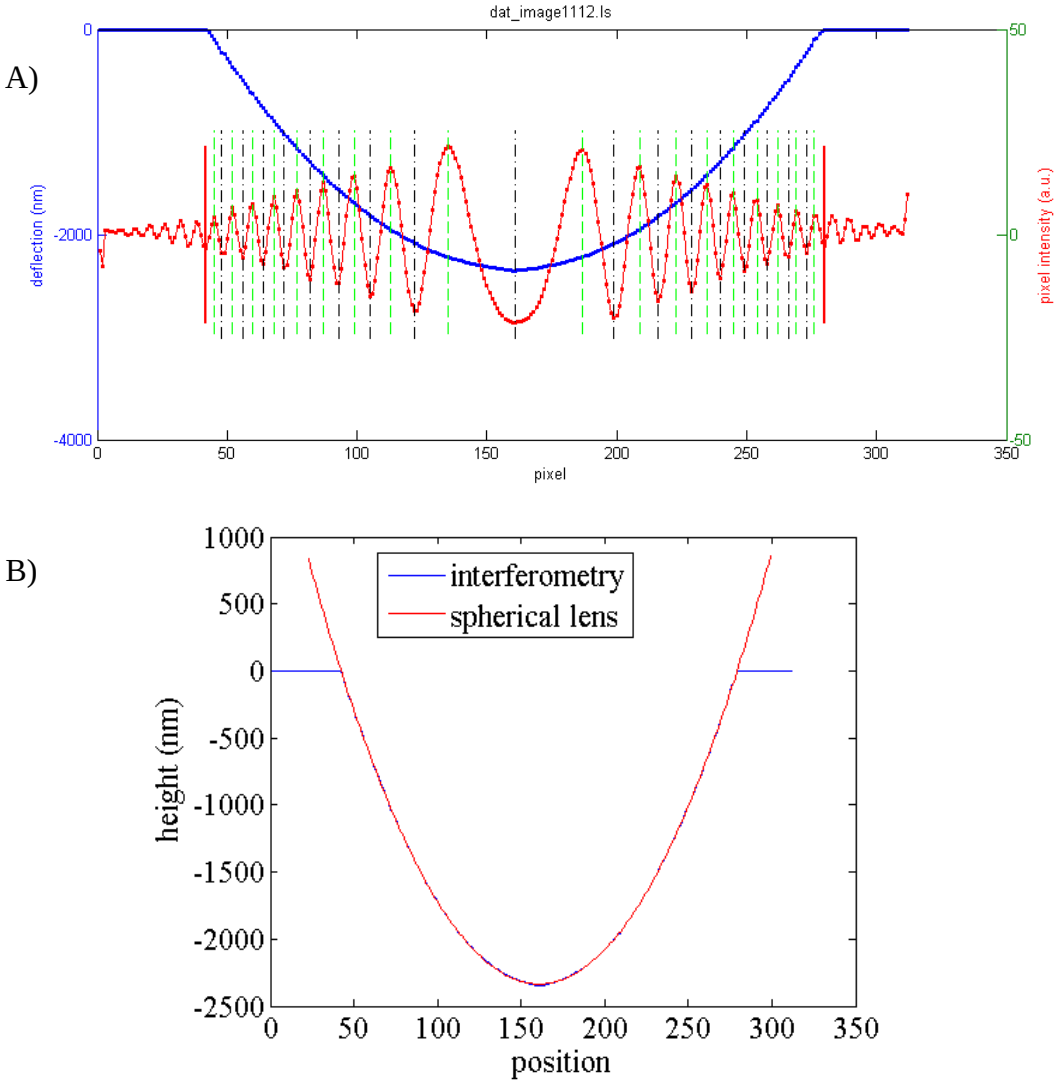

Figure 16: Analyzed image for spherical lens resting on a glass surface. The line scan was taken across the center of Figure 15 and averaged over 20 rows of the image. The region analyzed is bound by the two red bars with the positive extrema shown with dashed green lines and the negative extrema shown with dashed black lines. The calculated height profile matches the spherical lens profile very well.

A series of interferograms from a poly (butadiene) droplet approaching a glass substrate in a matrix of poly (dimethylsiloxane) is shown in Figure 17. The evolution of the drop topology is apparent in these images. The first image shows the droplet shape to be nearly spherical indicating that the shape has not been severely distorted by the surface yet. In the next image, the tip of the surface has blunted and the remaining images show the formation and growth of the dimple in the near contact region of the drop. This size of the dimple is small compared to the size of the drop (maximum ~3μm high compared to the image span of ~1mm). Once again the interferogram is essentially a contour map of the drop shape - constant height profiles are represented by fringe contours. The dimple profile is circularly symmetric, so a horizontal line scan was extracted from Figure 17F and, as seen in Figure 18, is used to obtain the dimple

deflection profile. An important caveat is that the fringes do not contain information on whether the deflection profile is upwards or downwards, or if the deflection slope has changed from positive to negative. This makes analysis of the drop topology more complex than for the glass lens above. The stationary points, where the height profile slope changes from positive to negative, need to be specified by the user. A similar example for the glass lens is that the center of the cross section was specified as a stationary point.

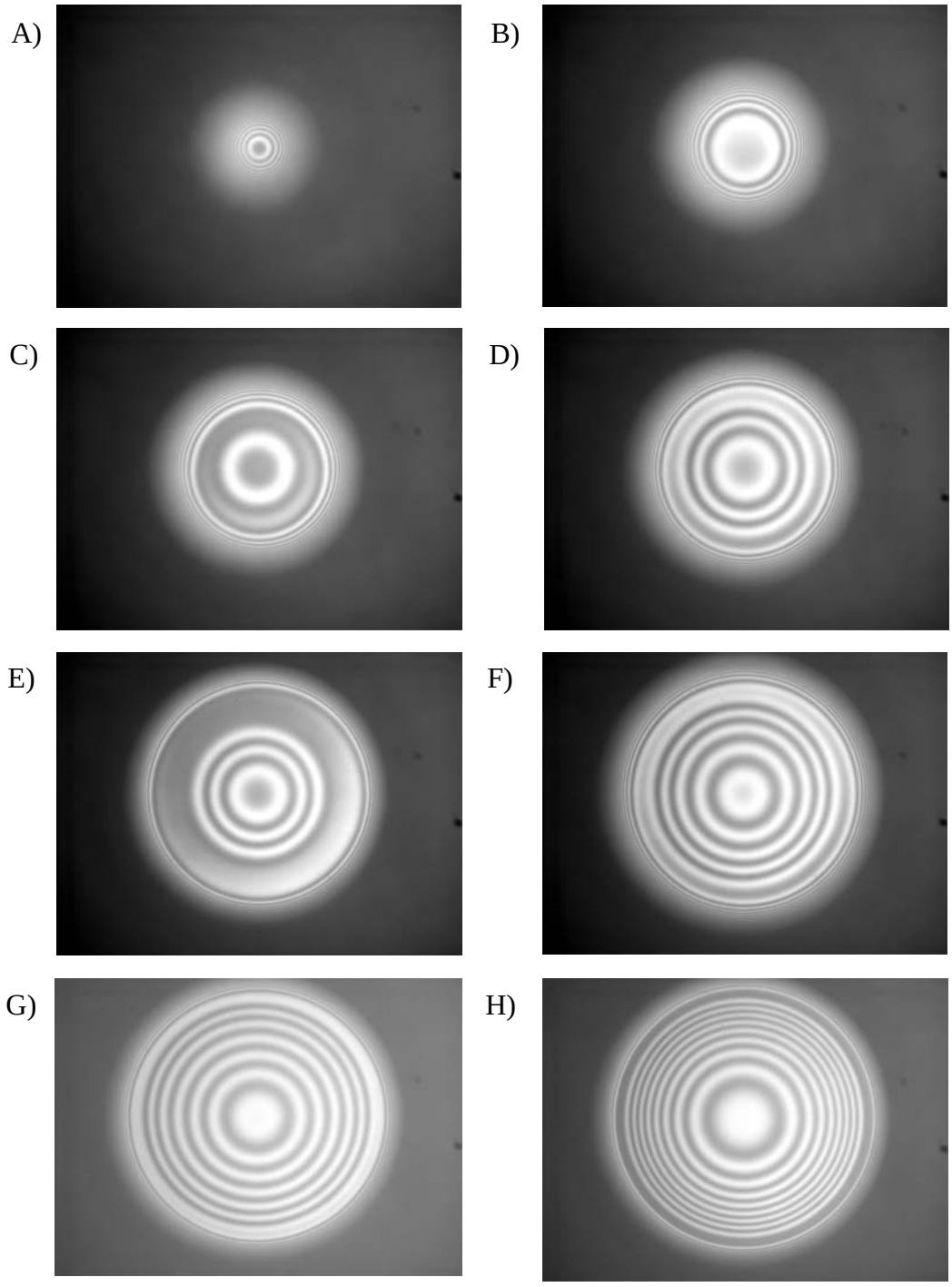

Figure 17: Interferogram series of a droplet approaching the surface. Image F was used to generate the linescan for Figure 18 below. Images (with frame number) are: A) t = -10 s (25), B) t = -7.5 s (35), C) t = -5 s (45), D) t = -2.5 s (55), E) t = 0 s (65), F) t = 2.5 s (75), G) t = 5 s (95), H) t = 30 s (186). Times are relative to image E which marks the start of the analysis shown in Figure 20.

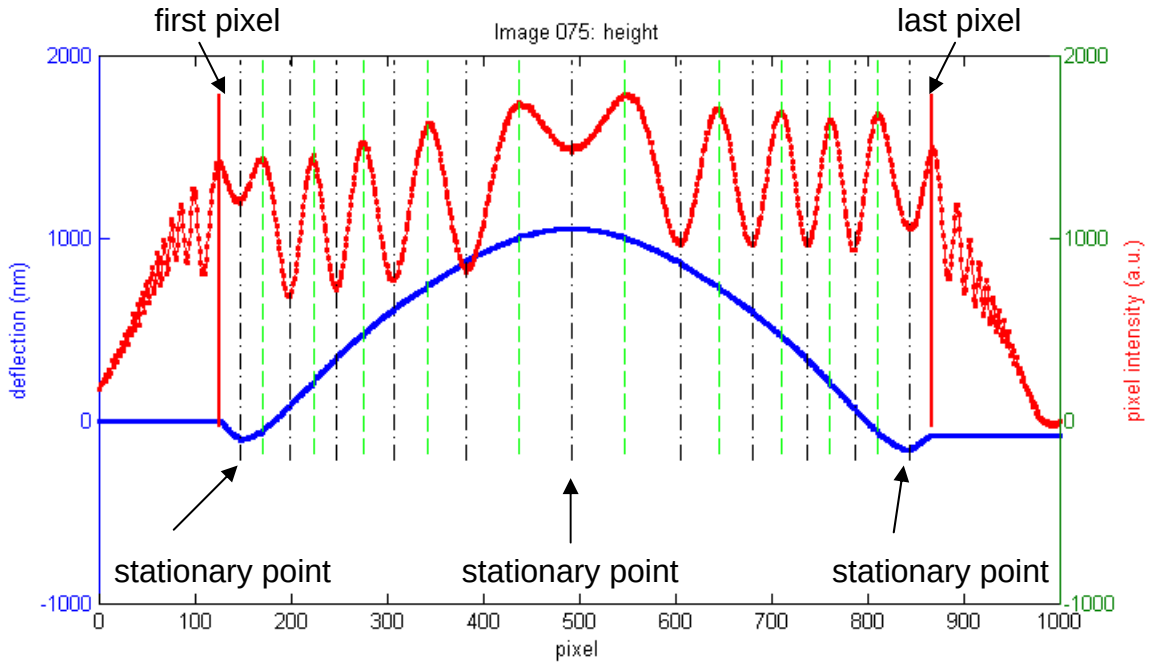

Figure 18: Linescan from Figure 17 above and the extracted deflection information.

Nonetheless, if the user has some information from the experiment, the droplet deflection profile can be extracted to ~10-30 nanometer precision from a single interferogram. For example, before the droplet approaches the substrate, it is round and there is a stationary point at its center and the local extreme can be assigned as a stationary point. Then, in most cases, the peak (or valley) at the stationary point does not reach an intensity as large (or small) as the neighboring extremes because the corresponding point on the drop interface is not an exact multiple of $\lambda/4$ from the surface. The data within this partial fringe does not range from a full minimum to a full maximum.

As the droplet continues to approach the substrate, a dimple begins to form. Then three stationary points need to be assigned as shown in Figure 18. At the edge of the droplet, the deflection profile is taken by convention to be downwards. Moving across the dimple, the profile turns upwards until the top of the dimple is reached, and then goes downwards until it reaches the end of the dimple where it finally goes back upwards.

Figure 19 shows the locations of all of the stationary point positions and intensities from all images in the interferogram series. For most images, there are three stationary points as indicated in Figure 18. The stationary point in the center has a relatively constant location while the other two stationary points break off from the center one when the dimple forms and move to the sides of the image. Over time, the stationary points map out interference fringes as their positions change relative to the glass surface. From Figure 19, we see that the average full fringe intensity range is consistently around 900. So for cases where the fringe is incomplete, we use instead the average full fringe intensity range as determined from Figure 19. For some images, the stationary point will not be clear from the data because as the droplet continues to move

downwards, the stationary point itself also goes through maxima and minima. Then, comparison with previous or subsequent images clearly shows which extreme is the correct location for the stationary point. In this case, the local data will represent a full minimum to maximum and therefore the average full range of fringe intensity need not be used.

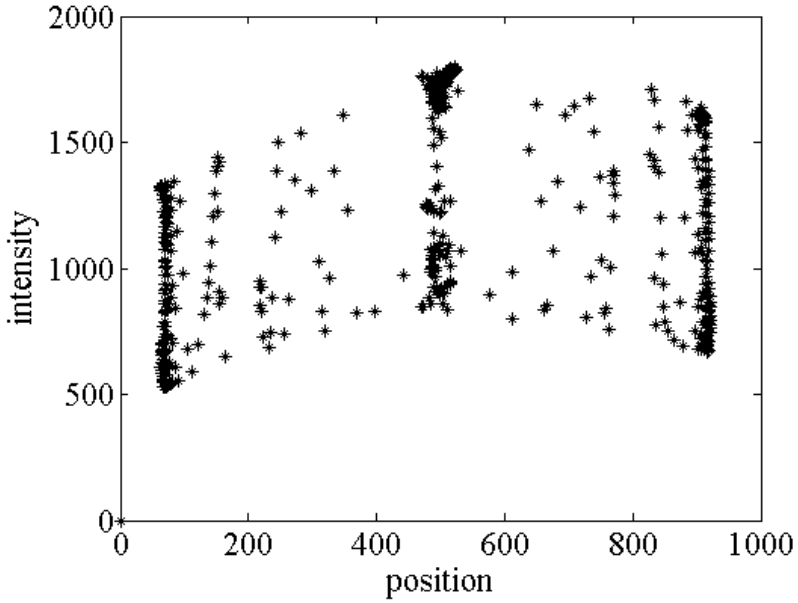

Figure 19: Graph of all of the stationary point positions and intensities for the interferogram series. Average fringe intensity range is around 900 for this series.

Based on these considerations, we developed an algorithm using Matlab (Mathworks, Inc. Lowell, MA) to extract droplet deflection profiles. The graphical output of the program is seen in Figure 18. The user selects the beginning and end pixels (vertical red lines) and also the stationary points (as indicated). Our program then finds maxima (green dashed lines) and minima (black dashed lines) using a nearest neighbor search. Using the phase unwrapping considerations based on the stationary points, it extracts the deflection profile (blue line in Figure 18). The algorithm finds the stationary point positions are at local extremes. Because the slope changes gradually at the stationary point positions in Figure 18, it is clear that their locations have been correctly assigned. A given image can be analyzed in about one minute. Individually generating the lines scans and analyzing a data set of 200 frames takes about a day. The deflection profiles from several interferograms frames can all be placed on one plot as shown in Figure 20. Here the data is shown once for every 2.5 s - 5 s (10-20 frames) as indicated on the right. In this case, the vertical offset between drop deflection profiles was set to 500 nm for clarity.

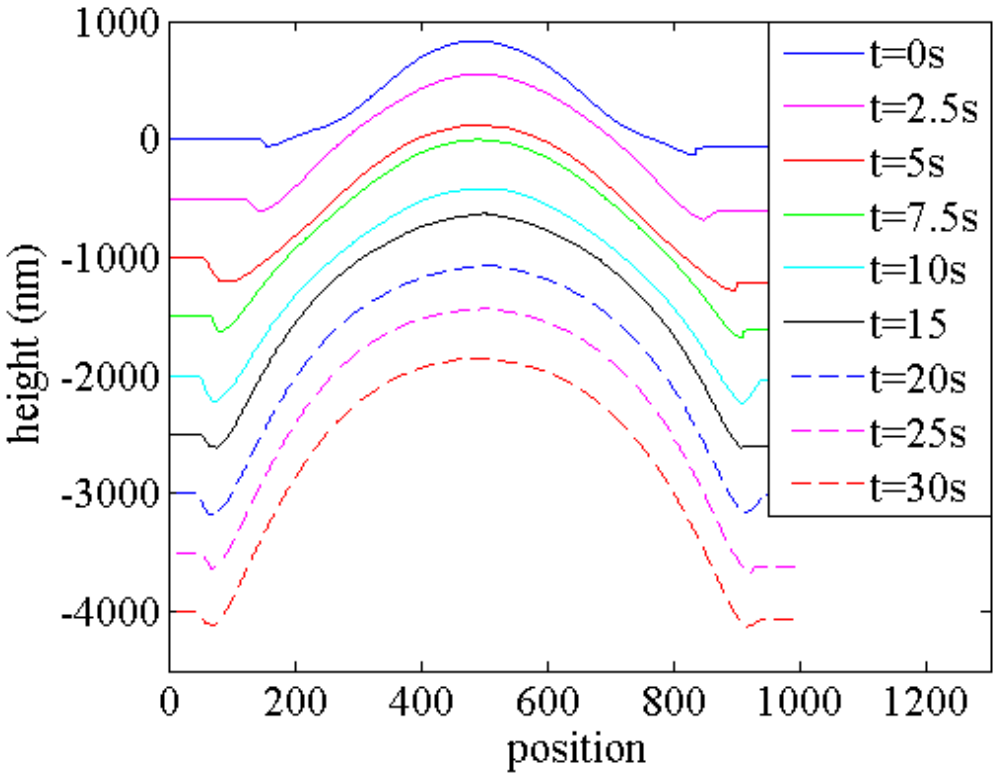

Figure 20. Dimple shape versus time as the drop approaches a flat surface.

We have also automated the process of analyzing the images. First all of the images are corrected for background lighting based on the initial image. The program finds the center of the image as the brightest point on the initial image and uses that image to calculate a correction for background lighting that is applied to every image. Line scans are performed across every image averaging over 20 rows of pixels and the resulting data are stored. Then, the height profiles are generated by working backwards from the last frame in the interferogram series. The user provides the locations of the stationary points for the last image and the average full fringe intensity range, and then the program uses those values as an initial guess for the preceding images. The program assumes that the stationary points in the preceding image are the extremes closest to or moving inwards from the previous location. If the positions of the stationary points move too far between frames, then the program stops to ask the user for help in identifying the correct stationary points. Generally the stationary points move smoothly but when they approach an extreme, they can be difficult to distinguish automatically. For the case shown in Figure 21, the stationary point is just a small shoulder on the side of a larger peak. In these cases the location is allowed to move to the next extreme which causes a small (and temporary) error in the peak height. Within a few frames the stationary point will reappear as a distinct extreme. User intervention is also required when a topology change occurs (i.e. the formation of the dimple causes a shift from one stationary point to three stationary points). Once the stationary points are found, the program crops the line scan data to include only one peak outside of the dimple region and performs the height analysis as described above. After one pass though the

series, the value of the average fringe intensity range can be determined, and the series is reanalyzed using the stationary point data recorded during the first pass. Using this automated system, a series of 200 frames can be analyzed in under an hour.

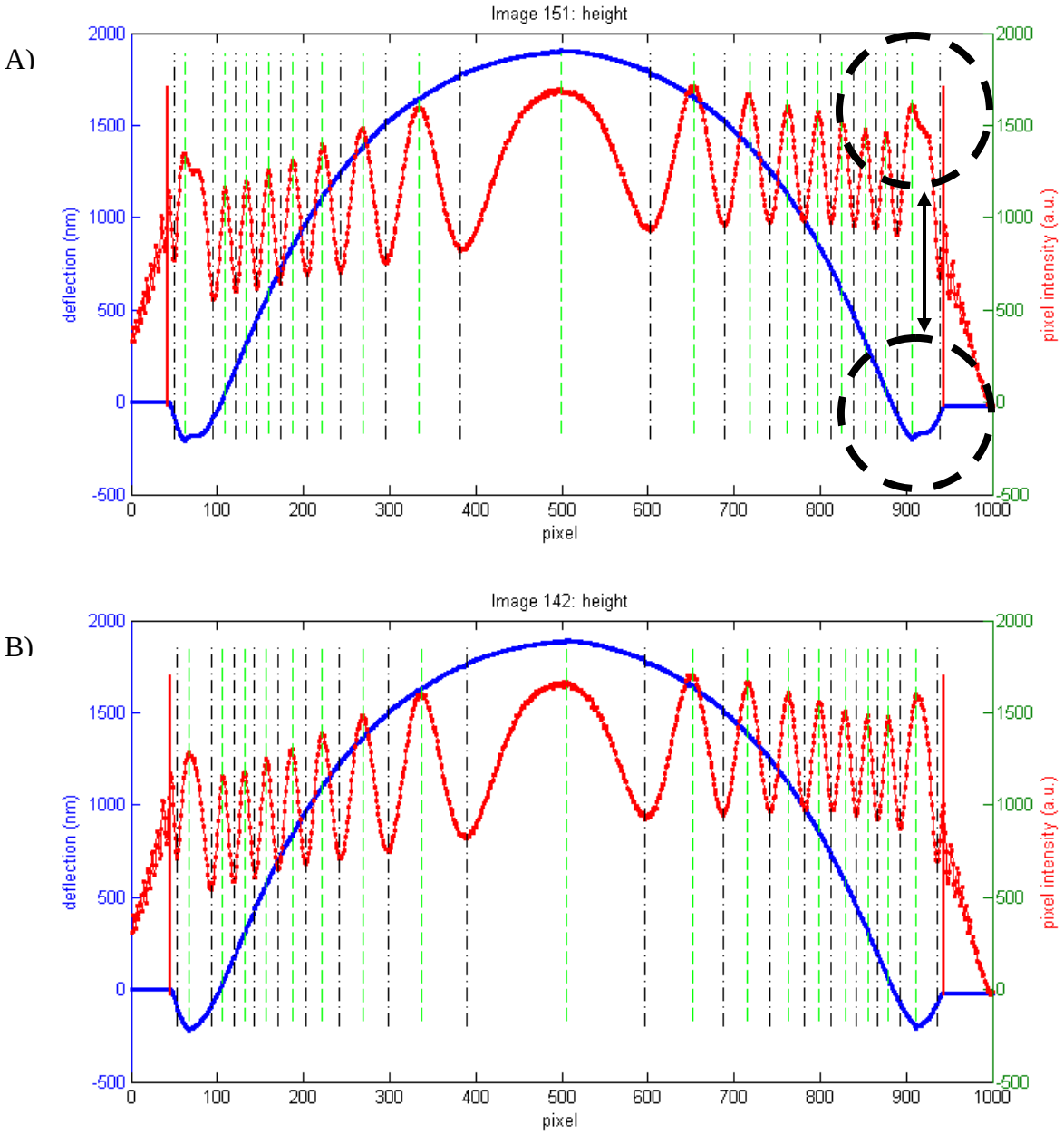

Figure 21: Example of the difficulty of finding the stationary point for frame 151 (A) where the stationary point is obscured by a neighboring peak. The true stationary point location is at the shoulder to the right of the peak. The algorithm subsequently recovers as shown in (B) so having the peak location jump to the neighboring peak causes only a temporary error in the calculated height function.

Up to this point we have treated the frames as individual images and only calculated their relative shapes. Using the intensities at the minimum gap (determined by the position of the stationary point), as shown in Figure 22, we can get information about the position of each image in the interferogram series relative to each other. By applying the same 'phase unwrapping' algorithm above to the intensity variation at the outer stationary point, we can determine the height offset between the individual frames in the series of images as shown in Figure 23. Then knowing the global location of the height at the minimum gap, the drop shape relative to the the rest of the images in the series can be calculated as a function of time as shown in Figure 24. It is interesting to note that during the dimple formation process, the height of the center of the drop remains relatively constant, thus the amount of fluid inside the dimple remains approximately constant. This occurs because the time scale for drainage of the thin fluid film is longer than the timescale of formation of the dimple. However, unless the drop coalesces, the displacement of the drop from the surface is only known to within a constant shift of $\lambda/4$.

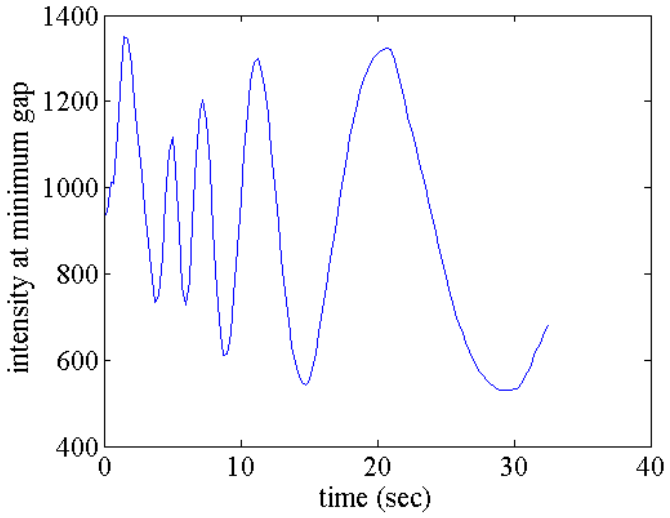

Figure 22: Intensity at the minimum gap height for the interferogram series shown in Figure 20. Data has been smoothed by averaging nearest neighbors.

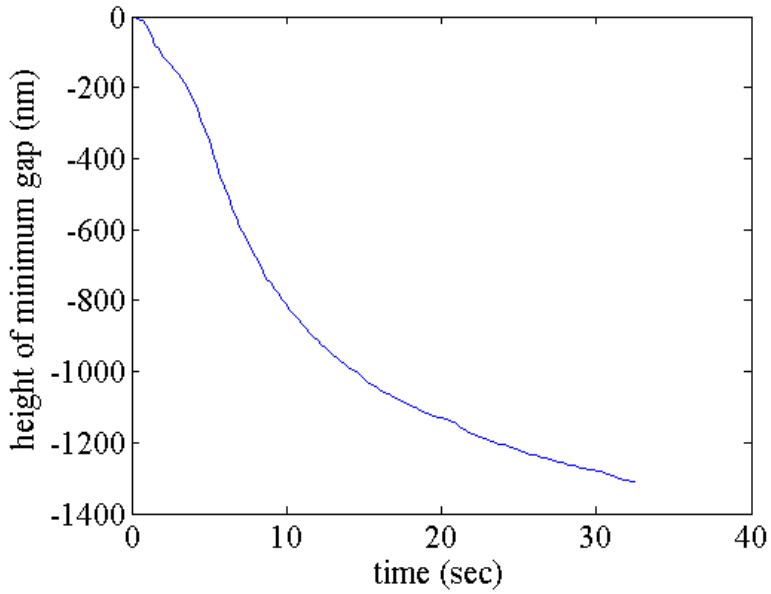

Figure 23: Minimum gap height as a function of time determined from the image intensity at the left stationary point.

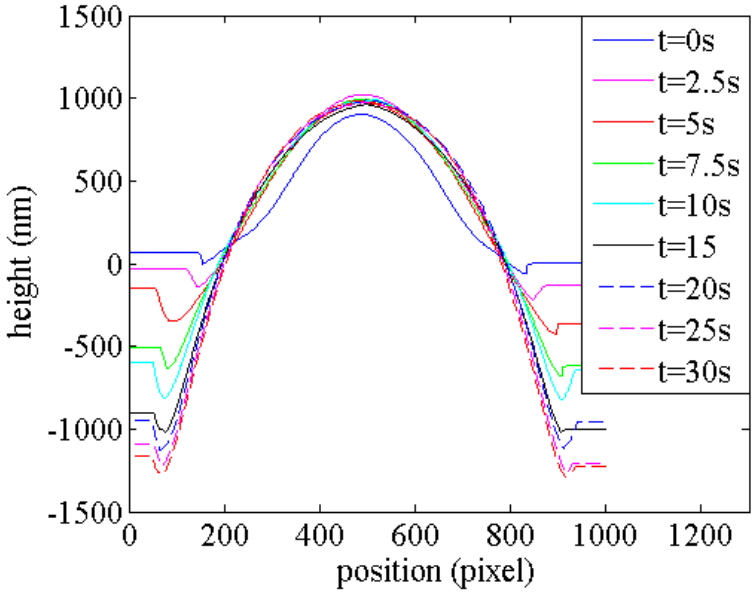

Figure 24: Absolute shape of the dimple region as the drop approaches the surface. Even though the drop is still approaching the surface, the amount of fluid trapped in the dimple is relatively constant because the dynamics of the drainage are slow.

4. CONCLUSIONS

We have developed a series of diagnostics to determine the effect of hydrodynamic forces on coalescence dynamics. We were able to design, build and characterize a computer controlled flow cell which allows a drop to be carefully positioned in the middle of a biaxial compressional flow. A simple modification would allow a switch to uniaxial extension flow. We have demonstrated that we can accurately track and position a drop in the flow. Then using particle image velocimetry, we showed that when the flow control is active, that the flow is symmetric and uniform. The radial uniformity of the flow is very good in the center of the flow around the position of the drop.

Additionally, we developed an interferometry capability to measure the drainage of the thin liquid film which forms prior to coalescence. We were able to confirm that our experimental system was effective for interferometry, having the right refractive indices to generate good contrast images and high enough viscosity to allow study of the formation and drainage of the dimple feature. We developed a semi-automated image analysis capability which takes the interferogram image series and allows the calculation of the absolute shape of the drop interface.

Unfortunately during the last six months of this two year project, laboratory operations were severely disrupted due to a major equipment move. We are now in a position to complete our goal of measuring the effect of hydrodynamics on coalescence by simultaneously measuring the film thickness using interferometry for a drop being steered by the control algorithm in the flow control chamber. We expect to complete these experiments by the end of the year.

5. REFERENCES

1. M. B. Nemer, X. Chen, D. H. Papadopoulos, J. Blawzdziewicz and M. Loewenberg. Phys. Rev. Lett. v92(11) (2004) p.114501.
2. S. Yiantsios and R. Davis. J. Fluid Mech. v217 (1990) p.547.
3. S. Guido and M. Simeone. J. Fluid Mech. v357 (1998) p.1.
4. K. Hool, R. Saunders and H. Ploehn. Rev. Sci. Instrum. v69 (1998) p.3232.
5. A. Zadrakov, G. Peters and H. Meijer. J. Colloid Inter. Sci. v106 (2003) p.195.
6. T. Chuang and R. Flumerfelt. Rev. Sci. Instrum. v68 (1997) p.3839.
7. E. Hecht. Optics, 3rd ed. Addison-Wesley, New York, 1998.
8. G. R. Fowles, Introduction to Modern Optics, 2nd ed. (Holt, Rinehard and Winston, Inc., New York, 1975).
9. D. Goodall, M. Gee, G. Stevens, J.Perea and D. Beagelhole. Coll. Surf. A v143 (1998) p.41.
10. J. E. Greivenkamp and J. H. Bruning, Phase Shifting Interferometry, in Optical Shop Testing; Vol. Chapter 14 of Second ed., edited by D. Malacara (J. Wiley & Sons, New York, 1992), pp. 501-598.
11. Y. W. Stegeman Time Dependent Behavior of Droplets in Elongational Flows (2002) PhD Thesis, Technische Universiteit Eindhoven, Eindhoven, Netherlands.
12. http://www.texloc.com/closet/cl_refractiveindex.html
13. K. Marinova, T. Gurkov, O. Velev, I. Ivanov, B. Campbell and R. Borwankar. Coll Surf. A v123 (1997) p155.
14. Y. Kaufman, D. Tanré and O. Boucher. Nature v419 (2002) p.215.

DISTRIBUTION

2 Michael Loewenberg
Department of Chemical Engineering
Yale University
PO Box 208286
New Haven, CT 06520-8286

1 Thomas Dimiduk
230 Risley Hall
Cornell University
Ithaca NY 14853

1	MS0734	J. Bruce Kelley	06215
1	MS0734	Margaret E. Welk	06219
1	MS0824	Wahid Hermina	01510
4	MS0834	Anne M. Grillet	01513
1	MS0834	Chris J. Bourdon	01513
1	MS0834	Leslie M. Phinney	01513
1	MS0834	Daniel J. Rader	01513
1	MS0834	Carlton F. Brooks	01512
1	MS0834	Tim J. Ohern	01512
1	MS0834	Robert D. Tachau	01512
1	MS0834	Steven Trujillo	01512
1	MS0836	Ken Chen	01514
1	MS0836	Rick C. Givler	01514
1	MS0836	Andrew M. Kraynik	01514
1	MS0836	Joel S. Lash	01514
1	MS0836	Mario J. Martinez	01514
1	MS0836	Harry K. Moffat	01514
1	MS0836	Lisa A. Mondy	01514
1	MS0836	David R. Noble	01514
1	MS0836	Patrick K. Notz	01514
1	MS0836	Rekha R. Rao	01514
1	MS0836	P. Randall Schunk	01514
1	MS1069	Maarten P. De Boer	01769
1	MS1080	David Sandison	01749
1	MS1082	Allen D. Gorby	01513
1	MS1245	John A. Emerson	02453
2	MS9018	Central Technical Files	8944
2	MS0899	Technical Library	4536
1	MS0123	D. Chavez, LDRD Office	1011